The supersonic and low-speed flows past circular cylinders of finite length supported at one end

By D. M. SYKES

Department of the Mechanics of Fluids, University of Manchester*

(Received 11 August 1961)

The flow past circular cylinders of finite length, supported at one end and lying with their axes perpendicular to a uniform stream, has been investigated in a supersonic stream at Mach number 1·96 and also in a low-speed stream. In both streams it was found that the flow past the cylinders could be divided into three regions: (*a*) a central region, (*b*) that near the free end of the cylinder, and (*c*) that near the supported end. The locations of the second and third regions were found to be almost independent of the cylinder length-to-diameter ratio, provided that this exceeded 4, while the flow within and the extent of the first region were dependent on this ratio. Form-drag coefficients determined in the central region in the supersonic flow were in close agreement with the values determined at the same Mach number by other workers. In the low-speed flow the local form-drag coefficients were dependent on length-to-diameter ratio and were always less than that of an infinite-length cylinder at the same Reynolds number.

Introduction

The present study of the flow past circular cylinders of finite length was undertaken to determine the extent to which the flow over the central portion of such cylinders could be considered to be two-dimensional, and also to determine the main properties of the flows near the ends of the cylinders.

The two-dimensional flow past a circular cylinder with its axis perpendicular to a uniform stream has been investigated by many workers whose main aim was to determine the circumferential pressure distribution and the form-drag coefficient. The changes in these properties which occur with changes of Reynolds number in low-speed flow were described by Goldstein (1938) for Reynolds numbers up to 10^5, and by Polhamus (1959) for higher values. Gowen & Perkins (1953) described the changes which occur in high-speed flow over the velocity range from subcritical up to a Mach number of 3·0.

The total drag coefficients of cylinders of various length-to-diameter ratios were determined by Wieselsberger (1923) at a Reynolds number of $8{\cdot}8 \times 10^4$. These results, which were quoted by Goldstein, showed that the average drag coefficient per unit length of a cylinder of finite length-to-diameter ratio was always lower than that of an infinite cylinder in a two-dimensional stream; the results were extended to a Reynolds number of $1{\cdot}6 \times 10^6$ by McKinney (1960). Circular

* At present at The War Office, Armament Research and Development Establishment, Fort Halstead.

cylinders of finite length have been used as Pitot tubes in low-speed flows by many workers. A full survey of the literature describing this work was given by Winternitz (1955), who also found that, when the pressure orifice was more than two cylinder diameters from the tip or free end, the stagnation pressure coefficient was independent of tip shape and equal to the Pitot pressure coefficient for Reynolds numbers between 10^3 and 12×10^3; Livesey (1956) extended these results to a Reynolds number of $1{\cdot}2 \times 10^5$.

The flow field over the forward portion of a cylinder at a free-stream Mach number of 2·0 was calculated by Uchida & Yasuhara (1956) and found to be in good agreement with the measured pressure distribution. Kondo (1957), at the same free-stream Mach number, determined the stream function behind the curved bow shock of a cylinder and hence evaluated the circumferential pressure distribution near the stagnation point. The pressure distribution around cylinders of various length-to-diameter ratios at Mach numbers between 1·8 and 6·0 was also measured in a shock tunnel by Kim (1956). Gowen & Perkins investigated the pressure distribution at various positions along a cylinder fixed at one end in a stream at a Mach number of 1·98, and found that the distributions measured near the free end differed from those measured along the mid-section of the cylinder.

The end effects have been investigated in greater detail in the present work at a Mach number of 1·96 and in a low-speed flow. Length-to-diameter ratios of 6·42, 9·67 and 14·56 were used and the Reynolds numbers based on the diameter of the cylinders were $10{\cdot}4 \times 10^4$ in the supersonic flow and $8{\cdot}6 \times 10^4$ in the low-speed flow.

2. Experimental apparatus and method

2.1. *Supersonic flow*

A circular cylinder of outside diameter $d = 0{\cdot}307$ in. fitted with a flat end-cap, was mounted in an intermittent vacuum-operated supersonic wind-tunnel with a 5 by 4 in. working section. The cylinder was set with its axis vertical and perpendicular to the tunnel centre-line. By means of a suitable traversing gear, the length of the cylinder, L, lying within the working section could be set to any desired value and the cylinder could be rotated continuously. The free-stream Mach number was 1·96 and the Reynolds number was $3{\cdot}4 \times 10^5$ per inch.

Pressure orifices of 0·015 in. diameter lay along a generator of the cylinder at distances h from the free end and communicated through the cylinder with an absolute mercury manometer of accuracy $\pm$ 0·1 mm of mercury. Pressure readings were taken in detail near the free end and near the root of the cylinder. Near the root the distribution of stagnation pressure was determined at a number of positions where the full circumferential pressure distribution was not determined. This was achieved by setting a pressure orifice to face upstream and then increasing in small steps the length L of the cylinder which projected into the flow. This variation in L had no effect on the flow near the root provided that $L > 4d$.

Photographs of the flow past cylinders of various lengths were taken using a conventional two-mirror schlieren system. It is assumed that these photographs show the trace of the bow shock in the plane of symmetry, but care must be taken

in interpreting other phenomena which appear on the photographs as it is not possible to determine their location within the width of the working section from these photographs.

The angular variation of the surface pressure p_c was measured at various positions h when $L = 6{\cdot}42d$, $9{\cdot}67d$, and $14{\cdot}56d$. From the measured pressures p_c, a pressure coefficient $C_p = (p_c - p)/\frac{1}{2}\rho U^2$ was formed, where p, ρ, and U are the free-stream static pressure, density and velocity. C_p was found to be symmetrical about the forward stagnation point, $\theta = 0°$. The local form drag coefficient,

$$C_D = \int_0^{\pi} C_p \cos\theta \, d\theta,$$

was evaluated by graphical integration of the downstream component of C_p for each pair of values of (L, h) investigated.

Thom (1928) found that in low-speed flow the pressure gradient around the circumference of a cylinder produced a displacement of the effective centre of a pressure orifice towards the region of high pressure. An angular correction term $\Delta\theta = \delta/2d$, where δ is the diameter of the orifice, should be applied to the measured angular displacement of an orifice. In these experiments $\Delta\theta = 1°$ and so was neglected as this was the accuracy of determining angular displacements.

2.2. *Low-speed flow*

A circular cylinder, geometrically similar to that described in § 2.1 above, but of outside diameter $d = 1{\cdot}25$ in. giving a Reynolds number of $8{\cdot}6 \times 10^4$, was mounted in the 20 in. square working section of a low-speed open-return wind-tunnel. Pressure orifices of 0·020 in. diameter were drilled in the cylinder at positions geometrically similar to the supersonic flow model, and the lengths of the cylinder lying within the working section were selected in the same way. The angular variation of the surface pressure p_c at various positions h was measured with a vertical water manometer, when $L = 6{\cdot}42d$, $9{\cdot}67d$, $14{\cdot}56d$, and $15{\cdot}8d$, the latter value occurring when the cylinder fully spanned the working section.

With this model the angular correction term $\Delta\theta = \frac{1}{2}°$ and was neglected as before. It was necessary to correct the experimental results for the effects which solid and wake blockage had on the apparent free-stream conditions. Preliminary calibration of the tunnel showed that there was no static pressure gradient along the empty working section, and the correction for the static pressure gradient induced by the wake was found to be negligible.

The flow past a cylinder of length L standing upright from the floor of a square working section of height H is effectively the flow past the half-model of a cylinder of length $2L$ in a duplex-tunnel working section of width $2H$. Following Pankhurst & Holder (1952), we find that the solid-blockage correction term ϵ_s for a cylinder partially spanning a duplex tunnel is given by $\epsilon_s = 2{\cdot}0\pi d^2 L/2(2H^2)^{\frac{3}{2}}$, which in the present case, when L is in inches, gives

$$\epsilon_s = 0{\cdot}00024L. \tag{1}$$

For a cylinder completely spanning the working section, the solid-blockage correction term is given by

$$\epsilon_s = 0{\cdot}82(d/H)^2 = 0{\cdot}0032. \tag{2}$$

The difference between this term and that given by (1) when $L = 20$ in. produced a change of 0·3 % in the correction factor applied to the dynamic pressure. This was disregarded.

The wake-blockage correction term ϵ_w for a cylinder spanning the working section for a tunnel is given by $\epsilon_w = \frac{1}{4}dC_D/H \simeq 0{\cdot}018$, and it was assumed that, for a cylinder of length L in., the wake-blockage correction term is

$$\epsilon_w = 0{\cdot}018L/H = 0{\cdot}0009L. \tag{3}$$

The total blockage correction term is $\epsilon = \epsilon_s + \epsilon_w$ and, from (1) and (3),

$$\epsilon = 0{\cdot}00114L.$$

The corrected free-stream velocity $U = U_T(1+\epsilon)$, where U_T is the empty-tunnel speed, and if the empty-tunnel static pressure is p_{s_T}, then the corrected pressure coefficient C_p is

$$C_p = \frac{p_c - p_{s_T}}{\frac{1}{2}\rho U_T^2}(1-2\epsilon) + 2\epsilon,$$

where p_c is the pressure measured at the cylinder surface.

The local form-drag coefficients C_D were evaluated by graphical integration of the downstream components of the pressure coefficients as before. Throughout the experiments, $\frac{1}{2}\rho U_T^2$ was kept constant whilst L was varied, and so $\frac{1}{2}\rho U^2$ increased as L increased. Thus the effective free-stream velocity increased, and hence the Reynolds number referred to the diameter of the cylinder increased by about 1 % as L increased from $6{\cdot}42d$ to $15{\cdot}8d$. The experimental procedure adopted to determine the surface pressure distributions was the same as that described in § 2.1 above.

3. Experimental results

Surface pressure measurements were taken in both the supersonic and the low-speed stream when cylinders of length $L = 6{\cdot}42d$, $9{\cdot}67d$, and $14{\cdot}56d$ projected into the working section. The pressure distribution when $L = 9{\cdot}67d$ in the supersonic stream is shown in figure 1 and when $L = 6{\cdot}42d$ in the low-speed stream is shown in figure 2. These distributions are shown in a three-dimensional projection which indicates the shape of the pressure 'hill' around the surface of the cylinders. In this projection the cylinder was considered to be laid with its free end forward and the stagnation line lying in a horizontal plane. The surface of the cylinder was then unrolled from right to left, between $\theta = 0°$ and 180° and the pressures were plotted vertically above the points at which they were measured. The distributions for the other values of L were of the same general shape.

3.1. *Supersonic flow*

3.1.1. *General description of the flow pattern*

The pressures over the rear portion of each of the cylinders, i.e. θ greater than about 120°, were almost constant along the length and around the circumference of the cylinder, whilst over the forward portion the circumferential pressure distribution could be divided into three regions.

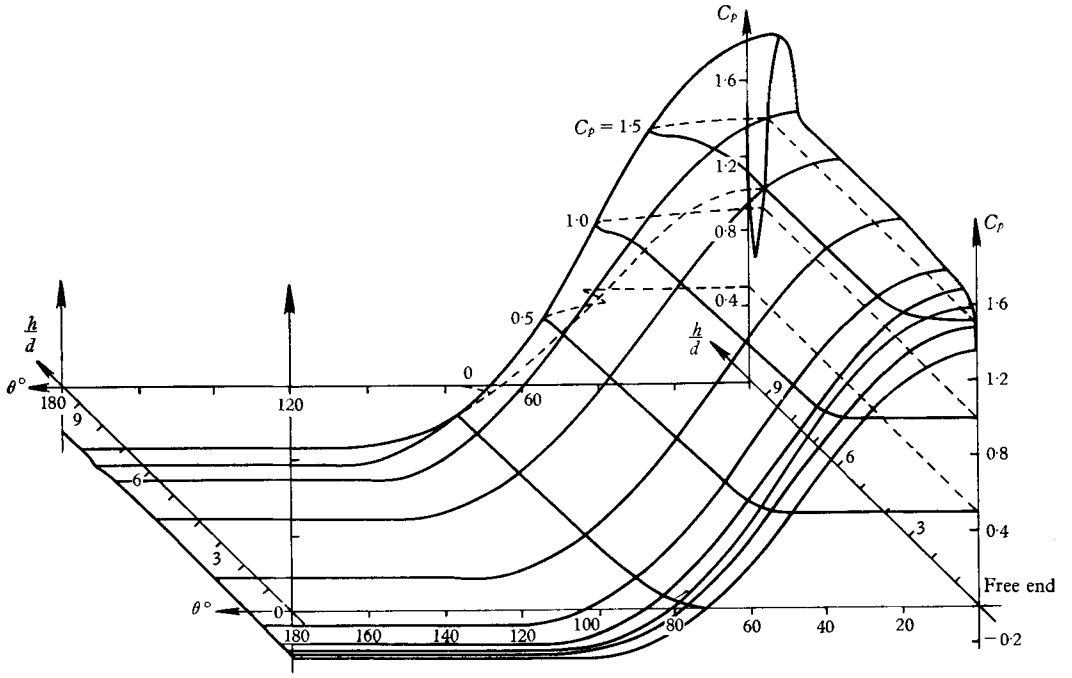

FIGURE 1. Pressure distribution on surface of cylinder; $L = 9{\cdot}67d$; $M = 1{\cdot}96$.

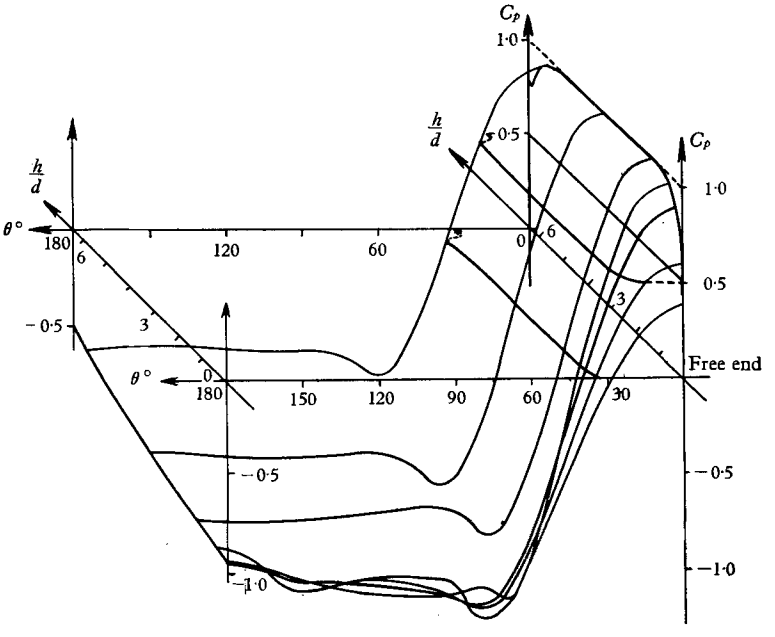

FIGURE 2. Pressure distribution on surface of cylinder; $L = 6{\cdot}42d$; low-speed flow.

The first (central) region, within which C_p depended on θ only, extended from about $2d$ below the free end to $2d$ above the root, and so its extent depended on L. The second (free-end) region extended for about $2d$ from the free end of the cylinder and here C_p varied with h as well as with θ. For constant values of θ, C_p increased with h until it attained the constant value found within the first region at the corresponding θ. The third (root) region extended for about $2d$ from the root of the cylinder and here C_p depended on the distance from the root, $r = L - h$, as well as on θ. Again considering constant values of θ, as r increased to $r = \frac{1}{3}d$ the pressure decreased to a minimum, and then it increased to a maximum at $r = 1{\cdot}6d$, after which it again decreased to the constant value found within the first region at the corresponding value of θ. The pressure distributions within the free-end and root regions appear to be independent of L for the three values used in these experiments.

Now considering the schlieren photographs of the flow past the cylinder $L = 9{\cdot}67d$, figure 3, plate 1 (the photographs of the flow when $L = 6{\cdot}42d$ and $14{\cdot}56d$ are similar), we see that the flow can be divided into three regions which correspond with the regions found in the surface pressure distribution. In the central region, which embraces the length of the cylinder excluding about $2d$ from either end, the trace of the bow shock in the plane of symmetry lies at an almost constant distance upstream of the stagnation line on the cylinder surface and the flow approximates to the two-dimensional flow past a circular cylinder. In the 'free-end' region, the bow shock bends towards the cylinder as the free end is approached. The root region arises from the interaction of the flow past the cylinder with the boundary layer on the nozzle liner. For small values of L ($L < 4d$) these two end effects overlapped and interacted with one another. For $L > 4d$ the flows in the two end regions appeared to be independent of L, as is seen from figures 4 and 5 which show the position of the bow shocks near the free end and the root of the cylinders for the different values of L.

3.1.2. *The central region*

In this region the bow shock in the plane of symmetry lay almost parallel to the forward stagnation line on each cylinder. The maximum circumferential pressure coefficients determined at $\theta = 0°$ at the various sections within this region were almost constant, $C_p = 1{\cdot}644 \pm 0{\cdot}005$, and independent of L. The pressure coefficients measured at $\theta = 180°$ are shown in figure 6 plotted against h with L as a parameter. These coefficients can be correlated with L to show that there was a slightly increasing pressure recovery over the rear portion of the cylinder as L increased.

The circumferential pressure distribution for $\theta > 120°$ was almost constant for the different values of (L, h). A small adverse pressure gradient was found on the surface of the cylinders in the region $110° < \theta < 120°$, which is the region in which the flow separated from the cylinder surface. Associated with this separation are a pair of weak shocks, which can be seen on photographs of the flow around a circular cylinder (e.g. Uchida & Yasuhara 1956) and it was these shocks which gave rise to the adverse pressure gradient. A typical circumferential pressure distribution determined in the present experiments is seen from figure 7 to be in

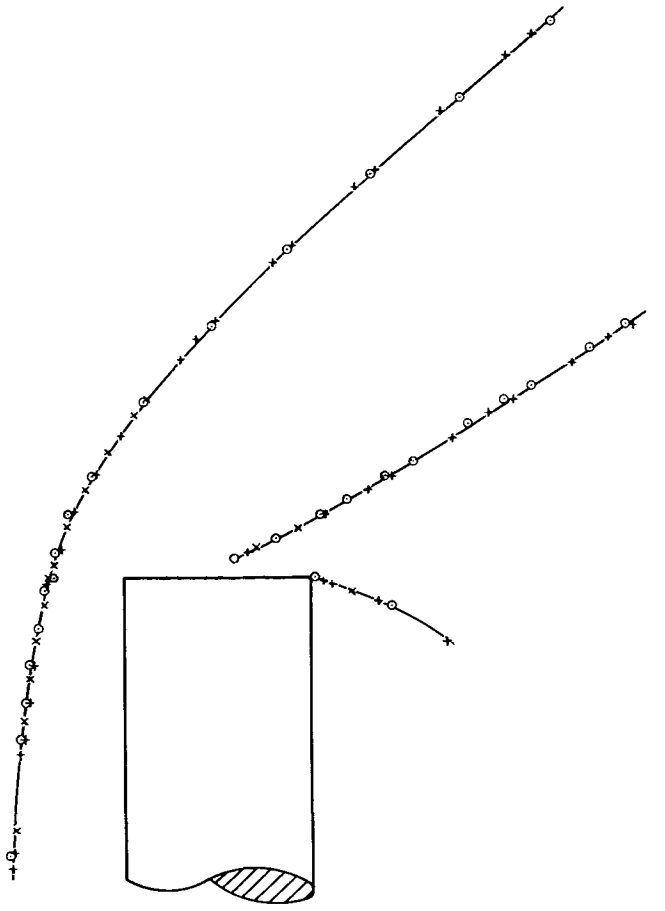

FIGURE 4. Free-end shock positions: +, $L = 6{\cdot}42d$; ⊙, $L = 9{\cdot}67d$; ×, $L = 14{\cdot}56d$.

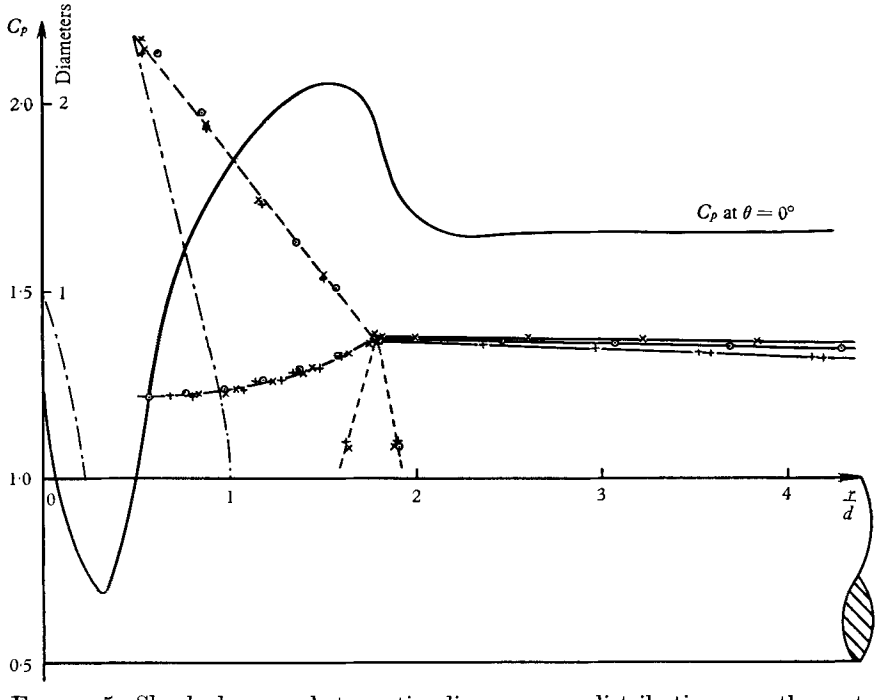

FIGURE 5. Shock shape and stagnation-line pressure distribution near the root: +, $L = 6{\cdot}42d$; ⊙, $L = 9{\cdot}67d$; ×, $L = 14{\cdot}56d$.

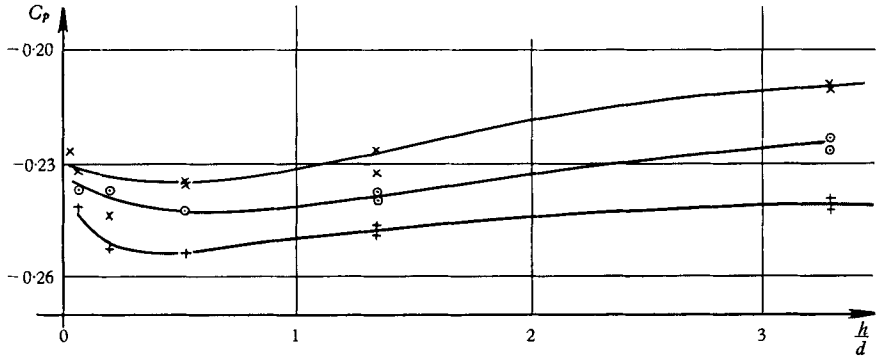

FIGURE 6. Pressure distribution at $\theta = 180°$ near the free end, $M = 1{\cdot}96$: +, $L = 6{\cdot}42d$; ⊙, $L = 9{\cdot}67d$; ×, $L = 14{\cdot}56d$.

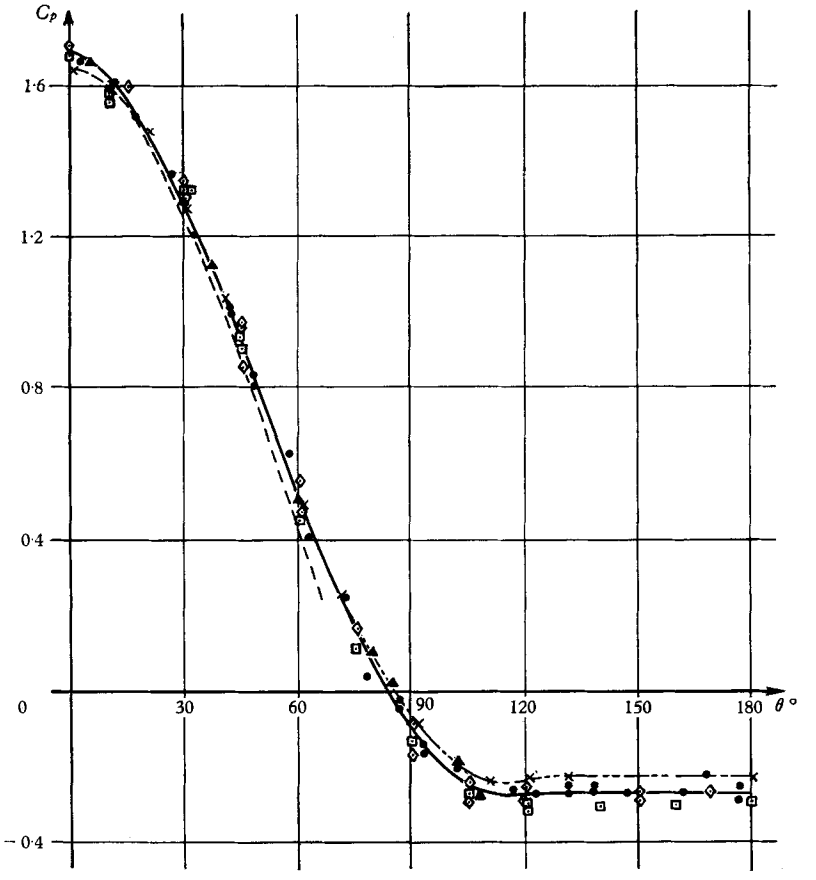

FIGURE 7. Comparison of circumferential pressure distributions. ——— Gowen & Perkins, $M = 1{\cdot}98$: ●, $R = 13{\cdot}2 \times 10^5$; ⊡, $R = 5{\cdot}5 \times 10^5$; ◇, $R = 1{\cdot}3 \times 10^5$. — — Uchida & Yasuhara, theory $M = 2{\cdot}0$; ▲, experiment $M = 1{\cdot}97$. -·-·- Present experiment: ×, $M = 1{\cdot}97$, $R = 1{\cdot}04 \times 10^5$.

close agreement with distributions determined by Gowen & Perkins and Uchida & Yasuhara.

The angular location of the sonic points over the surface of the cylinders, excluding the root region, was determined by assuming an isentropic expansion from the known stagnation pressure behind the bow shock. This is shown in figure 8 and is seen to vary with h near the free end but to be independent of L. Over the central region the sonic point lay at $\theta = 52°$ (cf. $\theta = 53°$ determined from the pressure distributions published by Gowen & Perkins). For $h < d$, the sonic

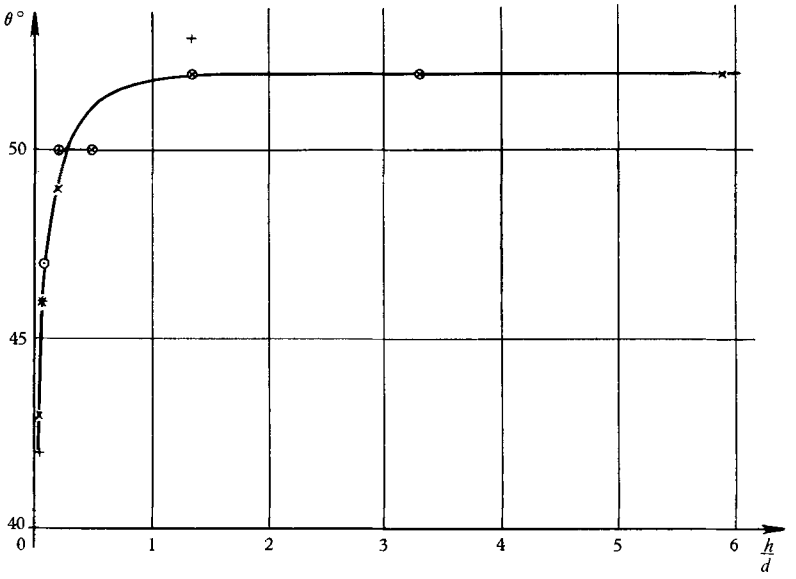

FIGURE 8. Angular location of the sonic point: +, $L = 6{\cdot}42d$; ⊙, $L = 9{\cdot}67d$; ×, $L = 14{\cdot}56d$.

point moved forward as the free end was approached, and at this end it lay at $\theta = 40°$. These axial sonic lines were connected at the free end by the sonic line which ran along the leading edge of the end-cap in the angular range $|\theta| \leqslant 40°$.

3.1.3. *The free end*

From figure 4 we have seen that the shape of the bow shock in the plane of symmetry was the same for the three values of L used in the experiment. Further details of the flow near the free end can be deduced from figures 3 and 9 which shows the pressure measured at $\theta = 0°$ in this region.

The flow approaching the end of the cylinder with an axial component was turned around the leading edge by an expansion fan. After experiments by Sharp (1959) we had expected to see a leading-edge separation bubble on the end-cap; although this was present, its profile could not be seen clearly since the leading edge was circular.

The surface pressure distributions over the end-cap were measured for the three lengths $L = 6{\cdot}42d$, $9{\cdot}67d$ and $14{\cdot}56d$, using three orifices of 0·015 in. diameter situated $\frac{1}{8}d$, $\frac{1}{4}d$ and $\frac{2}{5}d$ from the centre. The surface pressure contours are shown in

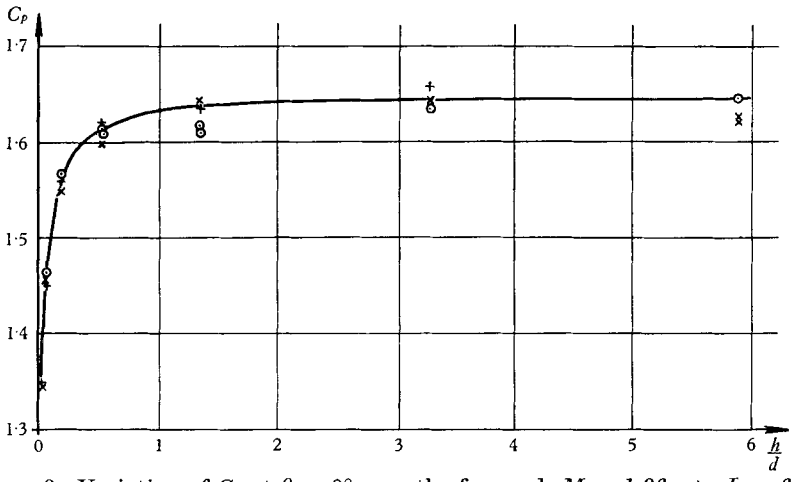

FIGURE 9. Variation of C_p at $\theta = 0°$ near the free end, $M = 1{\cdot}96$: +, $L = 6{\cdot}42d$; ⊙, $L = 9{\cdot}67d$; ×, $L = 14{\cdot}56d$.

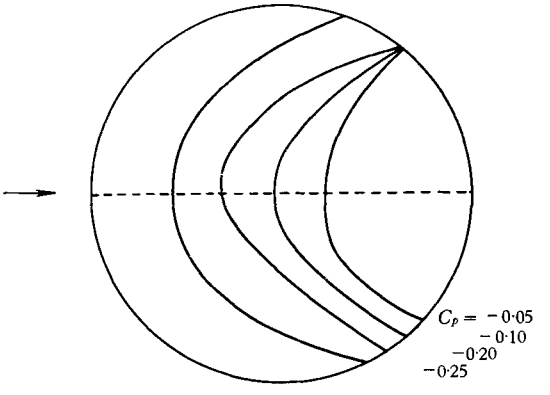

FIGURE 10. End-cap pressure contours, $M = 1{\cdot}96$, $L = 9{\cdot}67d$.

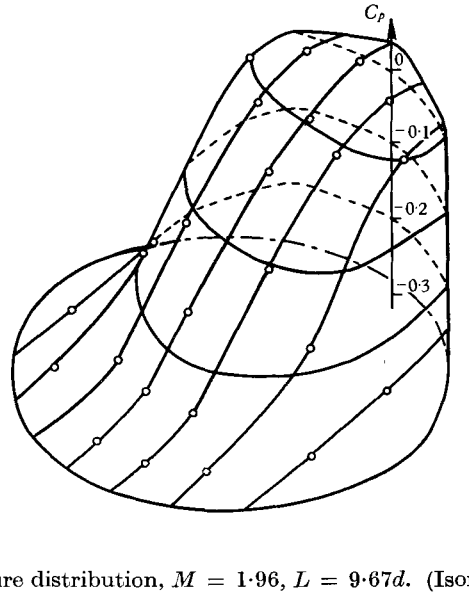

FIGURE 11. End-cap pressure distribution, $M = 1{\cdot}96$, $L = 9{\cdot}67d$. (Isometric projection.)

figure 10 and in isometric projection in figure 11 when $L = 6{\cdot}42d$; the contours for the other values of L were similar. These pressure distributions were almost symmetrical about the diameter lying in the incident flow direction, the slight asymmetry probably being caused by errors in aligning the end-cap. There is seen to be a region about $\frac{1}{5}d$ wide extending around the entire forward portion of the end-cap, within which the pressure was almost constant; this region was covered by the separation bubble.

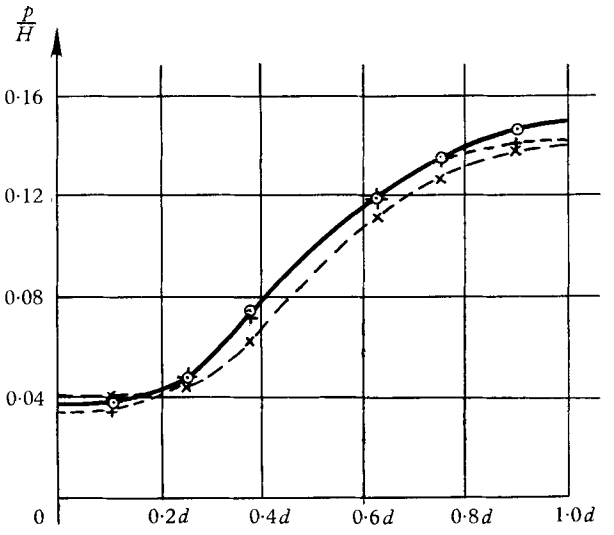

FIGURE 12. Pressure distribution along end-cap diameter of symmetry, $M = 1{\cdot}96$: +, $L = 6{\cdot}42d$; ⊙, $L = 9{\cdot}67d$; ×, $L = 14{\cdot}56d$; H = stagnation pressure.

The surface pressure distributions along the diameter of symmetry of the end-cap (figure 12) show that this constant low-pressure region was followed by a region of increasing pressure, caused by the reattachment of the flow at the downstream end of the bubble. This distribution, when $L = 9{\cdot}67d$, is compared in figure 13 with the pressure distribution near the leading edge of a flat plate measured by Sharp at the same Mach number. The same scales were used and the two pressure distributions were matched at a value measured in both experiments, to allow for the larger separation bubble present in Sharp's experiment.

The reattachment of the flow gave rise to the reattachment shock which is clearly visible in the schlieren photographs. The positions of the reattachment shocks were determined from the schlieren photographs and are shown in figure 4.

The pressures at the rear of the cylinders at the free end were lower than those near the trailing edge on the end-cap, so the fluid coming over the end-cap must have passed through an expansion fan at the downstream end, and so became directed slightly towards the root of the cylinder. The boundary layer from the end-cap can be seen moving in this direction after separating from the trailing edge; it appears to be rather thick, but this is due to its moving in different directions as it separates from the circular trailing edge. The pressures measured at $\theta = 180°$ on the cylinder initially decreased as h increased to $h = \frac{1}{2}d$ and then

increased steadily with further increase of h. This local minimum in the pressure was due to a vortex standing in the plane of flow symmetry, a secondary-flow effect in the separated-flow region on the downstream side of the cylinders.

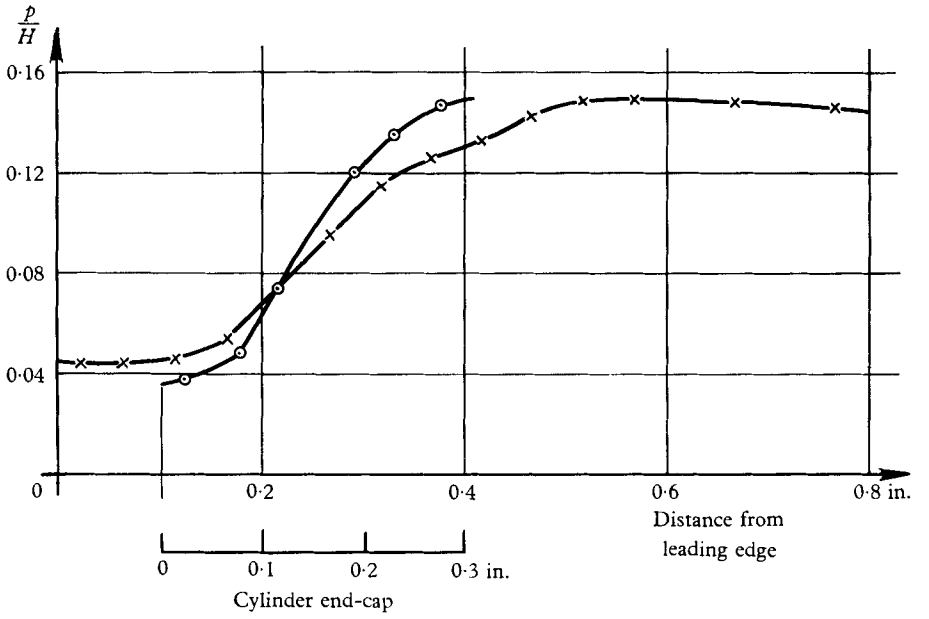

FIGURE 13. Pressure distribution along end-cap diameter of symmetry and near leading edge of flat plate, $M = 1{\cdot}96$: ⊙, cylinder $L = 9{\cdot}67d$; ×, plate.

3.1.4. *The root*

Near the root of the cylinders the bow shock terminated in a λ-form. The upsteam foot of this was due to the thickening and separation of the boundary layer on the nozzle liner, caused by the adverse pressure gradient in front of the cylinder and by the bow shock. The downstream foot was the continuation of the bow shock which was bent in the downstream direction at the triple point of the λ, thus moving towards the surface of the cylinder as it approached the nozzle liner.

The axial distribution of the maximum circumferential pressure coefficient near the root of the cylinder, shown in figure 14, was obtained by varying L and using two pressure orifices, situated at $h = 5{\cdot}88d$ and $7{\cdot}55d$, so as to show whether or not the changes in L had any effect on these pressures. No systematic difference could be detected between the two pressure distributions. The cylinder was also set so that it spanned completely the test section of the tunnel ($L = 16{\cdot}19d$), so turning the free end into a second root end. The pressure distribution at $\theta = 0°$ was measured near this end using the various pressure orifices lying within $4d$ of the end, and is seen from figure 14 to be the same as that obtained by using the two orifices $h = 5{\cdot}88d$ and $7{\cdot}55d$. From figure 14 we also see that as we move away from the root of the cylinders to $r = \frac{1}{3}d$, the maximum pressure coefficient decreases from $C_p = 1{\cdot}2$ to $C_p = 0{\cdot}7$. It then increases steadily to attain a maximum of $C_p = 2{\cdot}05$ at $r = 1{\cdot}5d$, after which it decreases rapidly to the central-region constant value of $C_p = 1{\cdot}645$ at $r = 2{\cdot}4d$.

It might be thought that the behaviour of C_p near the root of the cylinder, i.e. the increase which occurred as the wall was approached, was due to air leaking into the test section through the small sealed gap between the cylinder and the nozzle liner, but this possibility was eliminated by tests at the free end when the cylinder completely spanned the working section. Examination of the horizontal knife-edge schlieren photograph (figure 3*b*) revealed the presence of separated

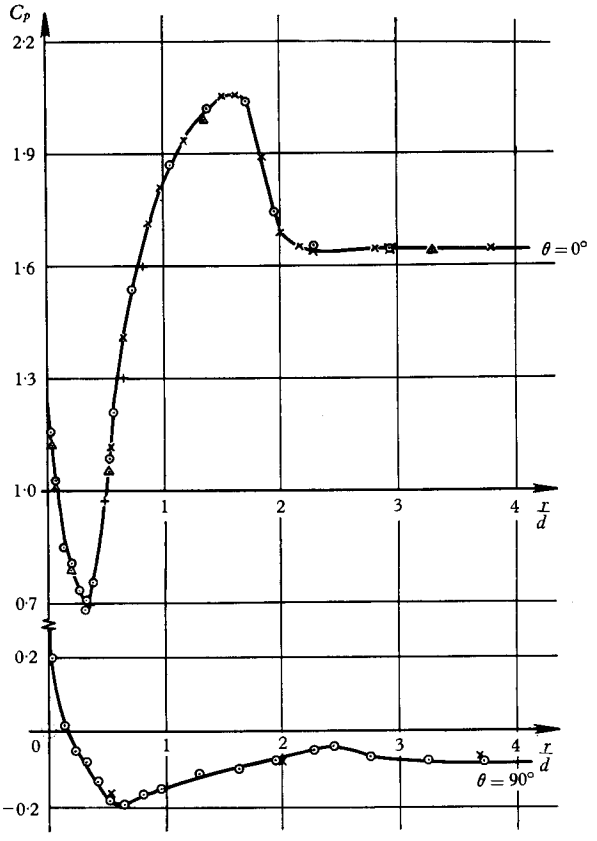

FIGURE 14. Pressure distribution at $\theta = 0°$ and 90° near the root of the cylinders and through the boundary layer (displaced $0{\cdot}3d$); $M = 1{\cdot}96$: ×, $h = 5{\cdot}88d$; ⊙, $h = 7{\cdot}55d$; △, $L = 16{\cdot}2d$; +, boundary layer.

flow in the region $r \leqslant \frac{1}{3}d$. The schlieren photographs did not show the extent of the separated-flow region across the test section, but it is thought that the region extended completely around the root of the cylinder. The photographs did show that the flow was separated downstream of the cylinder, but there was no indication of this in the pressure distributions determined at $\theta = 180°$ near the root. The axial pressure distribution at $\theta = 90°$ was determined using the orifice at $h = 7{\cdot}55d$ and is shown in figure 14; it is seen to behave in a manner similar to the pressure distribution at $\theta = 0°$.

The presence of a blunt body in a shear layer causes the streamlines in the fluid approaching the body to bend towards the region of low pressure. Thus the rise

in pressure as the root was approached was due to fluid from near the lower edge of the separated boundary layer being turned towards the root and then being brought to rest at the root. Little more could be deduced about the secondary flow in the separated region from the information available.

The Pitot pressure distribution through the boundary layer on the surface of the liner through which the cylinder passed was determined when the free end of the cylinder lay flush with the liner surface. The pressure coefficient increased from $C_p = 0{\cdot}70$ at $\frac{1}{30}d$ from the surface to $C_p = 1{\cdot}65$ at $0{\cdot}52d$: thus the boundary layer was approximately $\frac{1}{2}d$ thick.The pressure distribution through the boundary layer is shown in figure 14, assuming that the lower edge of the separated boundary layer meets the cylinder at $r = \frac{1}{3}d$. There is seen to be close agreement between this Pitot pressure distribution and the pressures measured on the cylinder at $\theta = 0°$ in the region $\frac{1}{3}d \leqslant r \leqslant \frac{5}{6}d$. Thus it is reasonable to assume that the pressures measured on the surface of the cylinder in this region were being measured through the separated boundary layer, as was indicated by the schlieren photographs and is shown in figure 5.

For $0{\cdot}5d \leqslant r \leqslant 1{\cdot}5d$, the trace of the bow shock in the plane of symmetry increasingly deviated from a normal shock, until at $r = 1{\cdot}5d$, just below the triple point of the λ-form, it passed through a point of inflexion. This increasing deviation from normal caused the pressure coefficient at $\theta = 0°$ to increase from $C_p = 1{\cdot}65$ at $r = \frac{5}{6}d$ to a maximum of $C_p = 2{\cdot}05$ at $r = 1{\cdot}5d$.

From figure 3*b* we see that the trace of the vortex sheet downstream of the triple point of the λ-form becomes very diffuse as it approaches the cylinder. If this vortex sheet were to remain as a thin sheet, as it would if the cylinder were not present, there would be a discontinuity in the pressure distribution on the cylinder. The adverse pressure gradient between the bow shock and the cylinder makes the vortex sheet unstable and causes it to spread axially. The density change through the vortex sheet occupies a region of similar extent to that occupied by pressure change and is seen in figure 5 to extend for nearly $\frac{2}{5}d$ at the cylinder in the plane of symmetry. In this region the pressure coefficient at $\theta = 0°$ decreased from its maximum value of $C_p = 2{\cdot}05$ at $r = 1{\cdot}5d$ to $C_p = 1{\cdot}70$ at $r = 2{\cdot}0d$; the pressure coefficient then increased slightly until finally $C_p = 1{\cdot}645$ at $r = 2{\cdot}4d$, after which it remained constant, being in the central region of the flow.

3.2. *Low-speed flow*

3.2.1. *General description of the low-speed flow pattern*

The pressures over the rear portion of each of the cylinders, i.e. $90° < \theta \leqslant 180°$ varied slightly with L, but for $\theta < 45°$ the pressure distribution showed that the flow could be divided into three regions, as in § 3.1.1 above.

In the central region C_p depended only on θ for $\theta < 45°$, but, for $\theta > 45°$, C_p varied with h and with L. In the second region, i.e. about $2d$ from the free end, for constant values of $\theta < 45°$, C_p increased with h until it reached the corresponding value found in the first region. In the third region, i.e. about $2d$ from the root, for constant values of $\theta < 45°$, C_p again depended on the distance from the root, r. Considering such a value of θ, C_p decreased to a minimum at $r = \frac{1}{8}d$ and then increased steadily to the constant value found within the central region at the

same value of θ. The extent of the two end regions appeared to be independent of L for the values used in this experiment.

The cylinder was also set to span the tunnel, $L = 15{\cdot}8d$, and then the distribution agreed with those determined at the root for the smaller values of L. The circumferential distribution of C_p and the value of C_D determined near the mid-point of this model agreed with those given by Goldstein at the same Reynolds number.

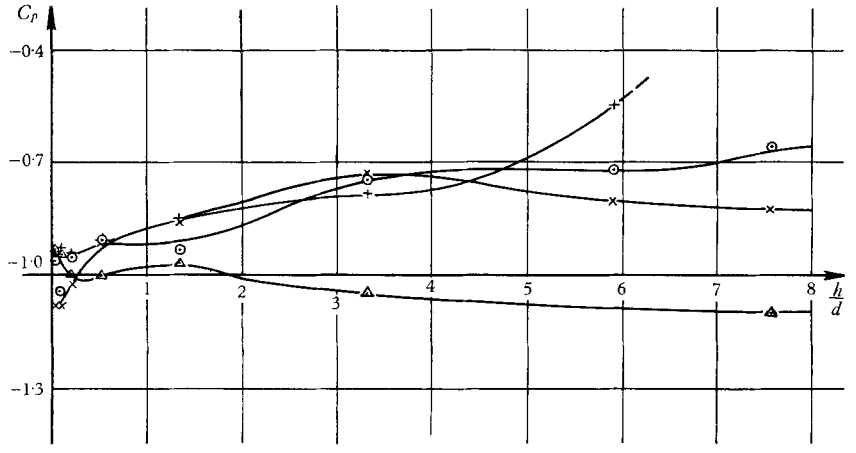

FIGURE 15. Pressure distribution at $\theta = 180°$, for low-speed flow: +, $L = 6{\cdot}42d$; ⊙, $L = 9{\cdot}67d$; ×, $L = 14{\cdot}56d$; △, $L = 15{\cdot}8d$.

3.2.2. *The central region*

In this region the circumferential pressure distribution over the forward portion of the cylinders, $\theta \leqslant 45°$, was independent of h and L, C_p decreased from a maximum, $C_p = 1{\cdot}00$, at $\theta = 0°$ to $C_p = 0$ at $\theta = 37°$ and reached a minimum at $\theta \simeq 70°$; this value depended on L and h. C_p then increased to a local maximum lying between $\theta = 80°$ and $\theta = 90°$ and for larger θ its behaviour depended on h.

When $L = 15{\cdot}8d$ the orifice $h = 7{\cdot}48d$ gave a pressure distribution which agreed with that given by Goldstein for a cylinder in a two-dimensional flow at the same Reynolds number. The pressure recovered at the rear of this cylinder varied axially, being a minimum at the mid-point and increasing towards the ends. This was caused by secondary flows between the boundary layers on the walls of the working section and the separated flow region at the rear of the cylinder.

Higher pressures were recovered over the rear of the cylinders when they did not fully span the working section. From figure 15 we see that the axial distributions of C_p at $\theta = 180°$ for these cylinders lie closer to one another than to the distribution when $L = 15{\cdot}8d$, and that as the length-to-diameter ratio decreased the pressures recovered over the rear of the cylinders increased.

3.2.3. *The free end*

Within $2d$ of this end the pressure coefficients at a given θ ($< 45°$) decreased as this end was approached; figure 16 shows the variation of C_p at $\theta = 0°$ plotted against h, with L as a parameter. The apparent variation of C_p with L is due to the

interference effect of the roof of the working section, which was not included in the overall blockage correction. The presence of the free end induced an axial velocity component v, directed towards this end, in the flow past the cylinder. The velocity

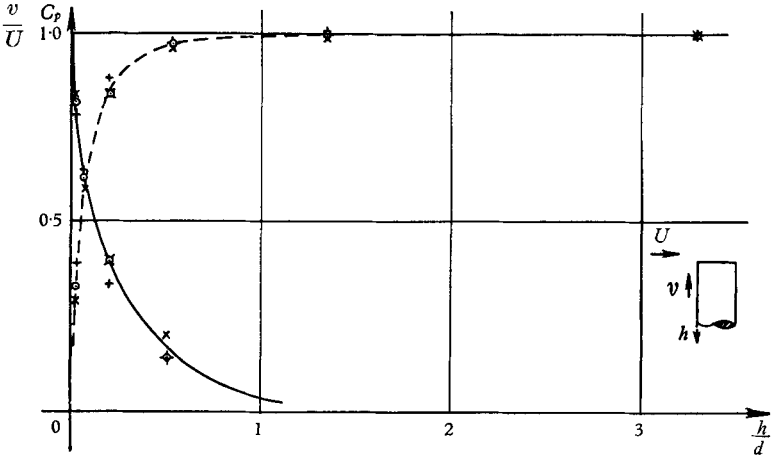

FIGURE 16. Pressure and velocity distribution near the free end, for low-speed flow, +, $L = 6{\cdot}42d$: ⊙, $L = 9{\cdot}67d$; ×, $L = 14{\cdot}56d$; — — — pressure; —— velocity.

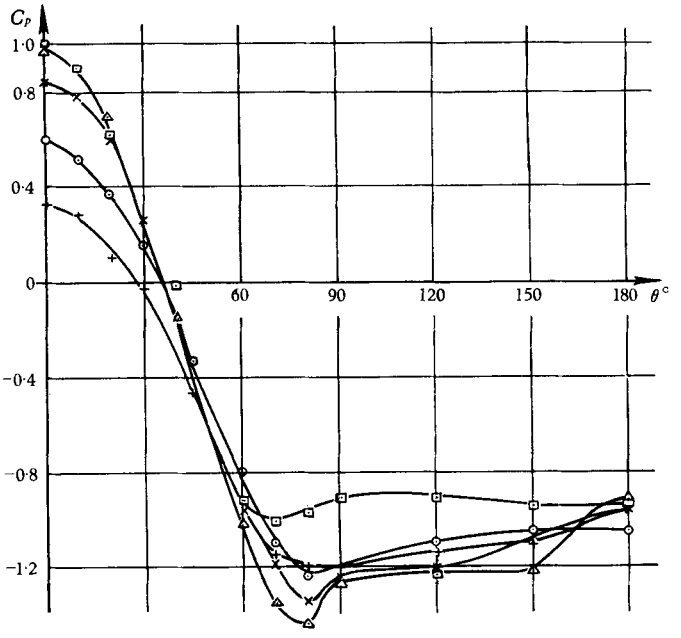

FIGURE 17. Circumferential pressure distributions when $h < 2d$, for low-speed flow, $L = 9{\cdot}67d$: +, $h = 0{\cdot}03d$; ⊙, $h = 0{\cdot}06d$; ×, $h = 0{\cdot}20d$; △, $h = 0{\cdot}52d$; ⊡, $h = 1{\cdot}35d$.

ratio v/U was evaluated from the pressure coefficients at $\theta = 0°$ and is seen, in figure 16, to increase from $v/U = 0$ for $h \geqslant 2d$ to $v/U \simeq 1$ at $h = 0$.

The circumferential distribution of C_p at various sections near the free end of the cylinder $L = 9{\cdot}67d$ are shown in figure 17; the distributions round the cylinders $L = 6{\cdot}42d$ and $14{\cdot}56d$ were similar. The point of separation of the boundary layer

from the surface of the cylinder moved rearwards as h decreased. The pressures over the rear of the cylinder decreased as h increased to $h = \frac{1}{2}d$, and then increased steadily until $h \simeq 6d$, indicating the presence of a vortex similar to that described in § 3.1.3 above.

The pressure distribution over the end-cap was not determined.

3.2.4. *The root*

The axial distribution of C_p was measured near the root at $\theta = 0°$, 90° and 180° as described in § 3.1.1. above, using orifices at $h = 7{\cdot}48d$ and $13{\cdot}92d$, and is shown in figure 18. The large scale changes in L affected the pressures at $\theta = 90°$ and

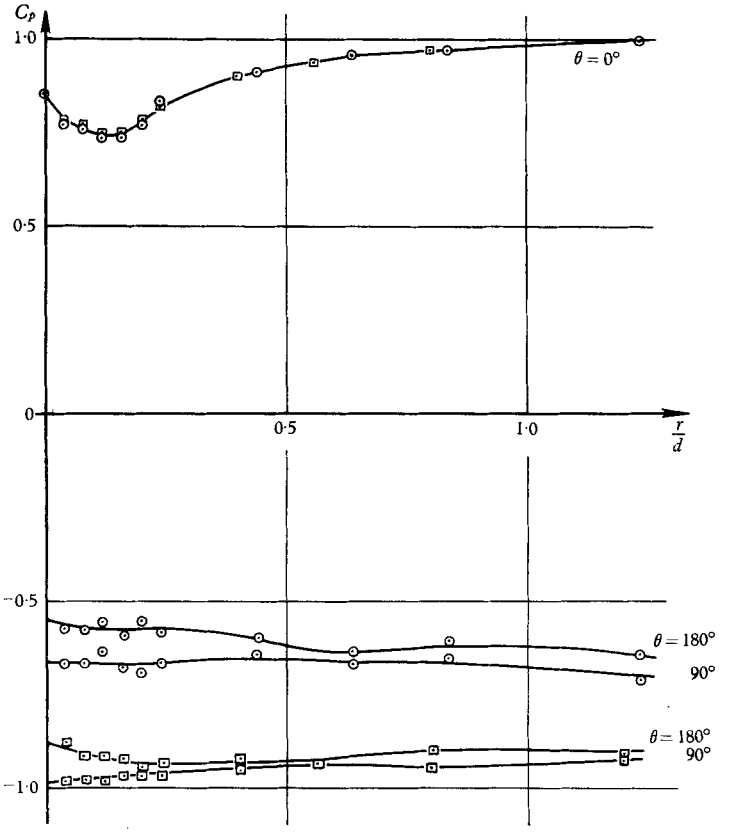

FIGURE 18. Pressure distributions at $\theta = 0°$, 90° and 180° near the root, for low-speed flow, with L varying: ⊙, $h = 7{\cdot}48d$; ⊡, $h = 13{\cdot}92d$.

180° as they affected the pressures over the rear in the central region of the cylinders; they had no effect on C_p at $\theta = 0°$.

This variation of C_p at $\theta = 0°$ near the root and also near the free end of the full-span cylinder $L = 15{\cdot}8d$ when this end lay in the boundary layer on the roof of the working section are shown in figure 19. This figure indicates separation of the boundary layer from the working-section floor by a vortex as was described in § 3.1.4 above. The vortex is swept downstream past the sides of the cylinder and separates from the cylinder between $\theta = 70°$ and $\theta = 80°$. Visual evidence of

a similar phenomenon occurring in low Reynolds number flow past a cylinder of small length-to-diameter ratio was found by Gregory & Walker (1950). Livesey also found evidence of similar flow reversal, i.e. the presence of a vortex, but near the roots of his cylinders the stagnation-line pressure coefficients were almost constant, indicating very little boundary-layer separation. However, the stagnation pressure gradients across the boundary layer in the present experiments were much greater than those in Livesey's experiments, and so there was a greater tendency for the boundary layer to separate and a stronger vortex to form in the present case.

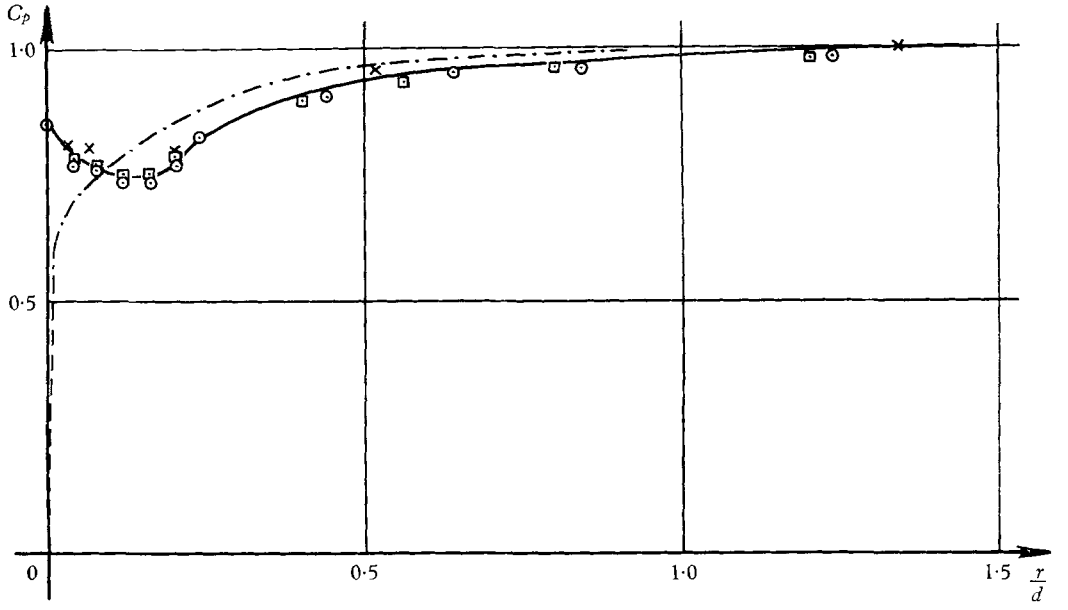

FIGURE 19. Pressure distribution at $\theta = 0°$ near the root and through the boundary layer, for low-speed flow: ⊙, $h = 7{\cdot}48d$; ⊡, $h = 13{\cdot}92d$; ×, $L = 15{\cdot}8d$; ·—· boundary layer.

The Pitot pressure distribution through the boundary layer was measured and is shown in figure 19. There is reasonable agreement between this pressure distribution and those measured at the front of the cylinder when $r > \frac{1}{5}d$ if the former is considered to be moved $\frac{1}{10}d$ away from the floor of the working section.

3.3. *Form drag*

The local form-drag coefficient C_D was evaluated at each position (L, h) by graphical integration of the downstream components of the pressure coefficients. The lateral distributions of C_D, plotted with L as parameter, are shown in figure 20 for the supersonic flow and in figure 21 for the low-speed flow.

In the supersonic flow C_D decreased at a given value of h as L increased, whilst in the low-speed flow C_D increased as L increased. This was due to an increase in L having opposite effects on the pressures recovered at the rear of the cylinders in the two flows.

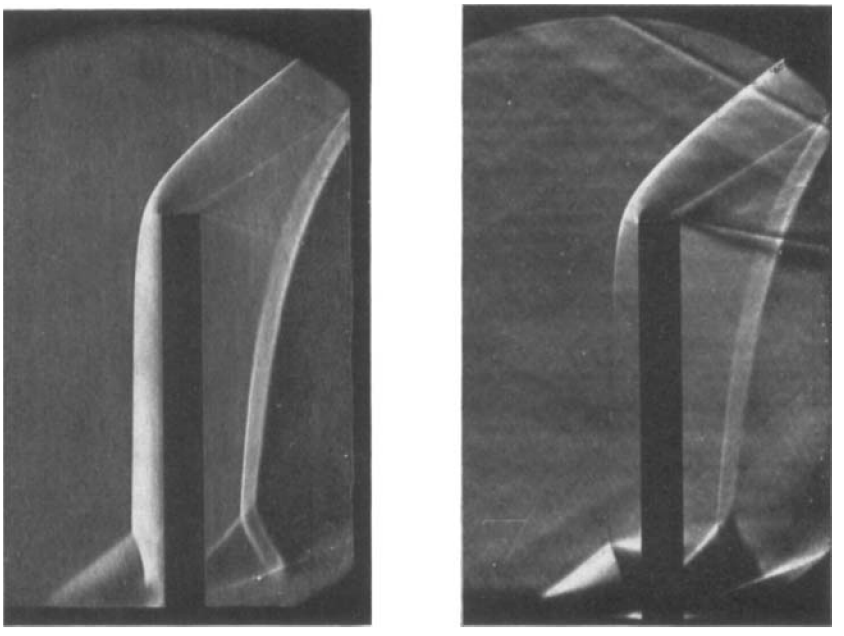

(*a*) Vertical knife edge (*b*) Horizontal knife edge

FIGURE 3. Schlieren photographs of the flow; $M = 1{\cdot}96$; $L = 9{\cdot}67d$.

Near the root of the cylinders in the supersonic stream the form-drag coefficient was evaluated at four positions (L, r). Since the flow in this region was independent of L for $L > 4d$, these coefficients are shown in figure 20 in their correct positions relative to the root of the cylinder for the three values of L, and the

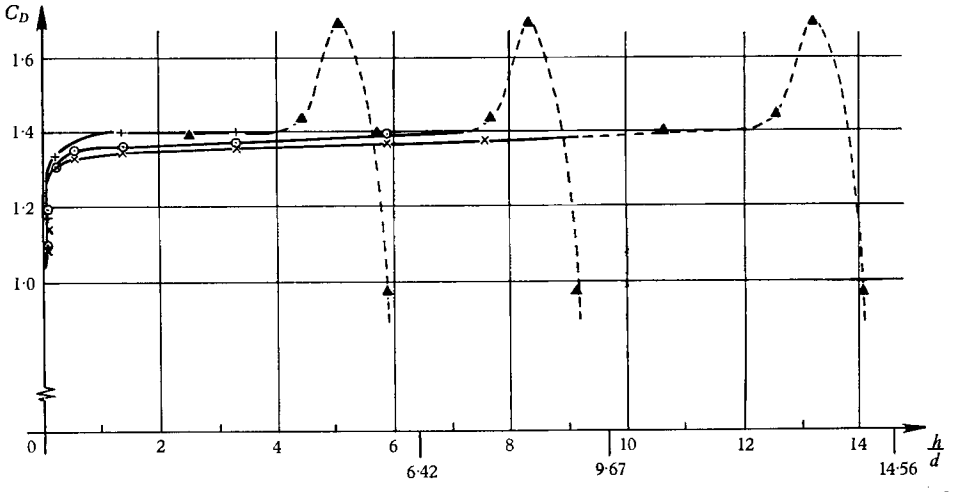

FIGURE 20. Lateral distribution of local form-drag coefficient, $M = 1{\cdot}96$: +, $L = 6{\cdot}42d$; ⊙, $L = 9{\cdot}67d$; ×, $L = 14{\cdot}56d$; ▲, root region for various L.

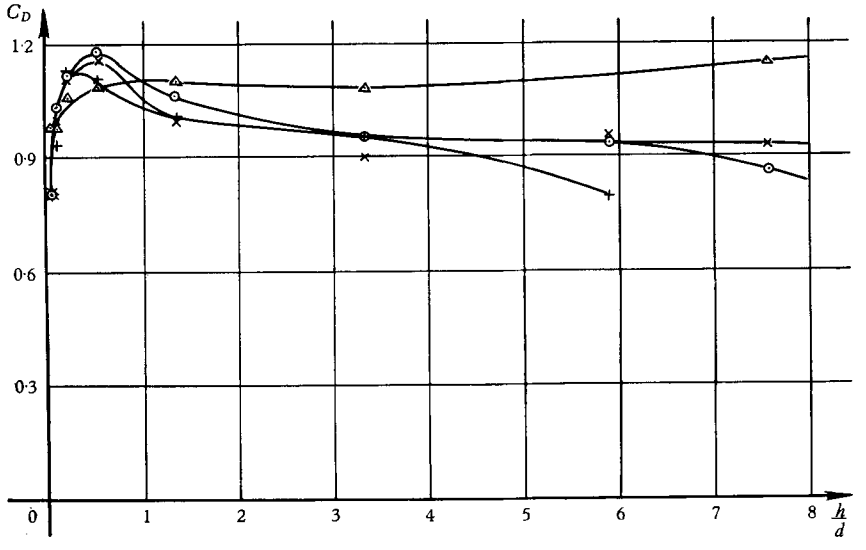

FIGURE 21. Lateral distribution of local form-drag coefficient for low-speed flow: +, $L = 6{\cdot}42d$; ⊙, $L = 9{\cdot}67d$; ×, $L = 14{\cdot}56d$; △, $L = 15{\cdot}8d$.

individual drag-coefficient curves are seen to extrapolate smoothly to meet this root distribution. It was not possible to do this in the low-speed flow since the pressures at the rear of the cylinder, and hence the drag coefficients, varied with L.

Gowen & Perkins found that Reynolds number effects were negligible and that, at $M = 1{\cdot}98$, the local drag coefficient varied between $C_D = 1{\cdot}41$ and

$C_D = 1{\cdot}42$ over the central region of a cylinder, with $L = 7{\cdot}5d$. From the present experiments the drag coefficients lay in the range $1{\cdot}37 \leqslant C_D \leqslant 1{\cdot}40$, the difference between the two sets of results being accounted for by the slightly higher pressures recovered over the rear of the cylinders in the present experiments.

In the low-speed flow, the average drag coefficient per unit length was not evaluated for the different values of L, but figure 21 indicates that this increases with L and shows agreement with previous results.

4. Comparison of the supersonic and low-speed flow patterns

Many points of similarity were found between the supersonic and the low-speed flow past circular cylinders of finite length supported at one end, when the length-to-diameter ratio exceeded 4. In both speed ranges, the major end effects each extended for about two diameters over the length of the cylinders, whilst the flow over the forward portion of the remainder of the cylinders was almost independent of the length-to-diameter ratio.

Near the free ends the streamlines were bent away from the root and it was generally found that the pressures measured in these regions were lower than those measured within the central regions at the same angular displacement. In all cases a vortex was found near the free end in the separated flow region on the downstream side of the cylinders. In the region near the roots of the cylinders, the boundary layer separated from the floors of the wind tunnels immediately upstream of the cylinders, and the streamlines from near the lower edge of the separated boundary layers rolled up and formed a horseshoe vortex slung around the roots of the cylinders. The Pitot pressure distributions through the boundary layer on the floors of the wind tunnels were found to be in close agreement with the pressures measured along the forward generators of the cylinders at a small distance from the roots. In the supersonic stream the flow near the root was independent of the length-to-diameter ratio of the cylinder, whilst in the low-speed stream, the pressures measured at the rear of the cylinders were dependent on this ratio.

The flow over the forward portion of the central regions of the cylinders was independent of axial position and length-to-diameter ratio, whilst the pressures measured at the rear of the cylinders were dependent on both these parameters; higher pressures were recovered with increasing distances from the free ends and increasing length-to-diameter ratio. This increased pressure recovery produced a corresponding decrease in the local form-drag coefficient and hence in the overall average drag coefficient per unit length, but this effect was not quite so large in the supersonic as it was in the low-speed flow cases.

5. Conclusions

The distributions of the local pressure and local form-drag coefficients have been determined for circular cylinders with length-to-diameter ratios of 6·4, 9·7 and 14·6 supported at one end in a stream at $M = 1{\cdot}96$ and in a low-speed stream. Reynolds numbers referred to the diameters of the cylinders were $10{\cdot}4 \times 10^4$ and $8{\cdot}6 \times 10^4$, respectively.

It was found that the flows could be divided into three regions: (*a*) the central region, (*b*) near the free end, and (*c*) near the fixed end or root. The flows in regions (*b*) and (*c*) were independent of one another and, in the supersonic stream, independent of the length of the cylinder provided the length-to-diameter ratio exceeded 4. These end regions were each about two diameters in extent.

In the supersonic stream, schlieren photographs and pressure measurements taken near the root of the cylinder revealed the details of the secondary flow phenomena. Over most of the length of the cylinders the local sonic point lay at $\theta = 52°$, but within one diameter of the free end it moved forward to $\theta = 40°$. Within the central region true two-dimensional flow past the cylinder was never achieved, but the flow gives a close approximation to that past a circular cylinder of infinite length as was shown by the agreement found between circumferential pressure distributions measured in this region, and those found by other workers at similar Mach numbers.

In the low-speed stream the whole flow was found to be dependent on the length-to-diameter ratio and this effect was attributed to changes in the local fluctuating flow field. Only when the cylinder fully spanned the working section did the circumferential pressure distribution measured in the central region agree with that given by other workers for the distribution in a two-dimensional flow at the same Reynolds number.

It was concluded that the drag coefficient of an infinite circular cylinder lying normal to a uniform supersonic stream at $M = 2{\cdot}0$ is $C_D = 1{\cdot}40 \pm 0{\cdot}02$.

The author wishes to thank Dr N. H. Johannesen and Dr J. H. Gerrard for their suggestions and advice, and the Department of Scientific and Industrial Research for a maintenance grant.

REFERENCES

GOLDSTEIN, S. 1938 (Ed.) *Modern Developments in Fluid Dynamics*, Vol. II. Oxford: Clarendon Press.

GOWEN, F. E. & PERKINS, E. W. 1953 *N.A.C.A. T.N.* 2960.

GREGORY, N. & WALKER, W. S. 1950 *Aero. Res. Coun., Lond., Rep.* no. 13436 (*FM* 1482).

KIM, C. S. 1956 *J. Phys. Soc. Jap.* **11**, 439–45.

KONDO, J. 1957 *Proc. 7th Jap. Nat. Cong. App. Mech.* 167–72.

LIVESEY, J. L. 1956 *J. Aero. Sci.* **23**, 949–55.

MCKINNEY, L. W. 1960 *N.A.S.A. T.N.* D-540.

PANKHURST, R. C. & HOLDER, D. W. 1952 *Wind Tunnel Technique.* London: Pitman.

POLHAMUS, E. C. 1959 *N.A.S.A. T.R.* R-29.

SHARP, A. W. 1959 *J. Fluid Mech.* **5**, 445–69.

THOM, A. 1929 *Aero Res. Coun., Lond., R. & M.* 1194.

UCHIDA, S. & YASUHARA, M. 1956 *J. Aero. Sci.* **23**, 830–45.

WIESELSBERGER, C. 1923 *Ergb. Aerod. Versuchsanstalt zu Göttingen*, **2**, 23–8.

WINTERNITZ, F. A. L. 1955 *Engineer*, **199**, 729–32.